



OPEN Combining an OSMAC approach and untargeted metabolomics to profile compounds exhibiting anti-HIV-1 activities in an endophytic fungus, *Penicillium Rubens* P03MB2

Neo Moloi^{1,7}, Mothusi C. Khumalo^{1,7}, Wonder P. Nxumalo^{2,3}, Sphamandla E. Mtambo⁴, Nompumelelo P. Mkhwanazi⁵ & Sizwe I. Ndlovu^{1,6}✉

The persistent burden of HIV-1 in Sub-Saharan Africa underscores the need for innovative treatments, as current antiretroviral therapies cannot eliminate latent proviral reservoirs and face challenges from multidrug-resistant strains. This study investigates the potential of *Penicillium rubens* P03MB2, an endophytic fungus from the *Albizia adianthifolia* plant, as a source of novel anti-HIV-1 compounds. The fungus was cultivated in various media (malt extract broth, oats, and rice), with oat media yielding crude extracts exhibiting significant anti-HIV-1 activity. Active fractions were further analyzed using an untargeted metabolomics and molecular networking approach, revealing clusters of secondary metabolites, including coumarins and other anti-HIV-1-associated compounds. A virtual screening workflow was employed to assess the binding affinities of these metabolites against HIV-1 protease. Furthermore, molecular dynamics simulations were used to analyze ligand-protein complex stability. Binding free energy calculations highlighted diosgenin as a promising candidate, with a binding free energy of -34.59 kcal/mol, outperforming the co-crystallized ligand ORV. This research demonstrates the potential of secondary metabolites from *Penicillium rubens* as novel anti-HIV-1 agents, offering a foundation for further developing effective antiviral therapies.

Keywords Anti-HIV-1 activity, Endophytic fungi, Human immunodeficiency virus; secondary metabolites, Untargeted metabolomics

The introduction of antiretroviral therapy has been transformative in the prognosis of HIV/AIDS, transitioning this pandemic into a manageable chronic illness¹. Despite the successes of combined antiretroviral therapy (cART) in reducing viral load, the currently available drugs cannot eliminate latently integrated proviral particles. Thus, the virus reactivates upon treatment interruption^{1,2}. In addition, the currently available cART drugs are slowly becoming ineffective due to emerging multidrug-resistant viral strains and severe side effects causing cytotoxicity to host cells and non-adherence to treatment³. Given these factors, there remains a need to search for novel alternative drugs with less toxicity that can escape these treatment barriers.

Microbial natural products from underexplored environments are gaining impetus as new sources of novel chemistries that cannot be produced through synthetic chemistry approaches. Microbial natural products are attractive in drug development programs due to their high rigidity, making them a suitable candidate for protein-protein interactions. This also fulfils the criteria for a new mode of action that is not susceptible to emerging drug resistance challenges^{4,5}. Endophytic microorganisms associated with medicinal plants qualify as an unexplored source and have been shown to produce a similar arsenal of bioactive natural products to their

¹Department of Biotechnology and Food Technology, Faculty of Science, University of Johannesburg, Johannesburg, South Africa. ²Department of Pharmacology, Faculty of Health Sciences, University of Pretoria, Pretoria, South Africa. ³NMISA, National Metrology Institute of South Africa CSIR Campus, Building 5, Meiring Naude Road, Brummeria Pretoria, South Africa. ⁴Scientific Services Division, Rand Water, PO Box 1170, Johannesburg 2000, South Africa. ⁵HIV Pathogenesis Programme, Doris Duke Medical research institute, School of Laboratory Medicine and Medical Sciences, University of KwaZulu-Natal, Durban, South Africa. ⁶Unit for Environmental Sciences and Management, North-West University, Potchefstroom 2520, South Africa. ⁷Neo Moloi and Mothusi C. Khumalo share first authorship. ✉email: sizwe.ndlovu@nwu.ac.za

plant hosts with higher therapeutic potential^{6,7}. Many small metabolites produced by endophytic fungi have been reported to exhibit antiviral properties⁷. For example, Bringmann et al.⁸ identified novel sorbicillinoid alkaloids, sorbicillatones A and B, from *P. rubens*. Sorbicillatone A demonstrated significant antiviral activity against HIV viral proteins. These studies suggest that *P. rubens* could be the source of novel anti-HIV compounds.

The challenge limiting the exploration of microbial natural products is that many remain undetected in culture media because they are encoded by biosynthetic pathways that remain silent or are expressed at lower levels⁹. Even when expressed, the complexity of crude extracts makes the chemical approaches to isolating and purifying these bioactive compounds complex and costly, often leading to the re-isolation of already-known compounds. One of the successful approaches in triggering the expression of silent biosynthetic pathways in microbial cultures is the OSMAC (one strain many compounds) approach, which involves systemic cultivation of microbial culture under varying conditions to simulate varying environmental triggers¹⁰. This, however, leads to complex crude extracts with a vast chemical space, making it difficult to decipher the compound(s) responsible for the observed activity¹¹. This can be addressed by following an untargeted metabolomics approach coupled with molecular networking, which clusters molecules with similar fragment ions into families, making further dereplication less complicated.

This study explores the power of combining the OSMAC approach with untargeted metabolomics in widening the chemical space in an endophytic fungus, *P. rubens* P03MB2. The resulting extracts were evaluated for antiviral activity. Furthermore, the compounds identified were analyzed in silico for binding to the target HIV protease, and molecular dynamics simulations were used to analyze the stability of the formed ligand-protein complexes.

Methods and materials

Production of secondary metabolites from *Penicillium rubens*

The fungal species explored in this study, *P. rubens* P03MB2 was isolated and stored as glycerol cultures from our previous study⁹. The fungal culture was revived on potato dextrose agar (Neogen corporation, United Kingdom) supplemented with 50 µg/mL chloramphenicol (Sigma Aldrich, SA), and incubated at 28°C for five days. For large-scale fermentation, 15 × 500 mL Erlenmeyer flasks were prepared and divided into five Erlenmeyer flasks per media for three different media: malt extract broth (90 mL) and 28 g each of oats media and rice media. For solid media fermentation, 100 mL of WOFT (K₂HPO₄: 0.5 g L⁻¹; yeast extract: 1 g L⁻¹; sodium tartrate: 0.5 g L⁻¹) was added to 28 g of rice and oats before the media was autoclaved¹². Mycelial plugs (6 mm²) were transferred under sterile conditions to all prepared media, and the flasks were incubated at 28 °C in the dark for 14 days.

Extraction of secondary metabolites from *Penicillium rubens*

After the incubation period, an equal amount of ethyl acetate (ACE chemicals, Johannesburg, South Africa) was added to each Erlenmeyer flask and placed on an orbital shaker at 24 °C with shaking at 150 rpm overnight before separating the organic layer from the aqueous layer. The recovered organic layer (ethyl acetate) was dried using a rotatory evaporator at 40 °C, and the solid extract was collected and resuspended in a 1:1 mixture of distilled water and methanol in 25 mL McCartney bottles. The crude extracts were partially purified using solid phase extraction (SPE) reverse phase chromatography to remove chromatography-impairing lipids and simplify the extracts into smaller fractions. Fractionation of the crude extracts was performed as described by Stoszko et al.¹³. Concisely, the dried material was reconstituted in 50% methanol (MeOH) to a concentration of 100 mg/mL. Subsequently, 1 mL of this suspension was spiked with 20 µL of phosphoric acid (Sigma-Aldrich, South Africa) and loaded onto MAX (mixed mode, strong anion-exchange) and MCX (mixed mode, strong cation-exchange) cartridges acquired from Waters Corporation (Prague, Czech Republic). The sorbent surfaces of the cartridges were desalted and eluted with an increasing stepwise gradient using methanol (5%, 45%, 95%) to extract the adsorbed compounds. The eluted fractions of organic compounds were evaporated to dryness at 40 °C through incubation. The dried fractions were reconstituted to 1 mg/mL in methanol (HPLC grade, Sigma Aldrich, South Africa) and stored at 4 °C until further use.

Evaluation of cytotoxicity of the crude extracts from *Penicillium rubens* using MTT viability assay

The crude extracts' cytotoxicity effects and cell viability were assessed using the CYQUANT MTT proliferation kit, following the manufacturer's instructions (Thermo Fisher, Waltham, USA). Briefly, a 96-well culture plate was seeded with 15,000 TZM-bl cells per well in 200 µL of DMEM and incubated at 37 °C with 5% CO₂. After cell attachment, 10 µL of *Penicillium rubens* crude extracts and the positive control drug Zidovudine (AZT) (NHI AIDS research and reagent program) at 300 µg/mL were serially diluted 10-fold from 300 µg/mL in DMEM containing 10% heat-inactivated fetal bovine serum, 50 µg/mL gentamycin, and 25 mM HEPES (LTC Biosciences, Gainesville, FL, USA) buffer in respective wells. The plate was then incubated at 37 °C with 5% CO₂ and 95% humidity for 48 h. Following incubation, the supernatant (treatment medium) was replaced, and each well received 10 µL of 12 mM MTT solution before incubation for an additional four hours at 37°C with 5% CO₂. Afterward, the MTT solution was discarded, 50 µL of 0.2% DMSO (dimethyl sulfoxide) was added to each well to dissolve the formazan crystals, and the plate was further incubated for 10 min at 37°C. The absorbance of each well was measured at 540 nm using the Victor Nivo microplate reader (PerkinElmer, MA, Waltham, USA).

The percentage of cell viability was calculated using the formula below²:

$$\%Cell\ viability = \frac{Sample\ absorbance - media\ control}{Mean\ media\ control\ absorbance} \times 100$$

Antiviral activity of the crude extracts from *Penicillium rubens*.

The crude extracts and fractions were prepared for activity testing by making a 3-fold dilution for each extract, starting at 300 µg/mL in DMEM in a 96-well flat-bottom plate. After that, 50 µL of diluted HIV-1 NL4.3 (MOI=0.05) virus was dispensed to all the wells except cell control wells and incubated for one hour at 37 °C, 5% CO₂. TZM-bl cells were prepared at a density of 1 × 10⁵ cells/mL in a growth media containing 37.5 mg/mL DEAE dextran and were seeded in a 96-well plate and incubated at 37 °C 5% CO₂ for 72 h. Zidovudine (AZT) at 300 µg/mL was used as a positive control, while the uninfected and untreated cells were used as negative controls. After incubation, the culture medium (100 µL) was replaced with new DMEM media, and a 100 µL of Bright Glo luciferase reagent (Promega, Madison, WI, USA) was added to each well under low light conditions. Following this, the cells were allowed to lyse before they were transferred to a 96-well bottom flat black plate (Costar, Corning Incorporated, USA), followed by incubation at 37 °C. The relative luminescence unit was measured immediately after incubation using a Victor 2 luminometer plate reader (Perkin-Elmer Life Sciences, Shelton, CT) at 540 nm. The percentage of viral inhibition was expressed following this equation: % HIV inhibition = [(Average Sample-Average Control)/(1-(Average Viral Control-Average Control))] × 100 (2) The half-maximal inhibitory concentration (IC₅₀) causing morphological changes in the HIV inhibition dose-response curve by 50% was calculated using GraphPad Prism Software (v.5).

High-resolution liquid chromatography-mass spectrometry analysis

The selected bioactive crude extracts and fractions were analyzed on a Nexera LC-40D XR liquid chromatography hyphenated to a quadrupole time-of-flight (Q-ToF) tandem mass spectrometer (LCMS-9030 qTOF, Shimadzu Corporation, Kyoto, Japan) following a method described by Ramabulana et al., (2021) with some modifications. The separation was performed using a 2.7 µm particle size Shim-pack Velox C18 column (150 mm, 2.1 mm, Shimadzu Corporation, Kyoto, Japan) at 40°C. All samples were injected at a volume of 20 µL with solvent A (0.1% formic acid, Merck, Darmstadt, Germany) and solvent B (acetonitrile: 0.1% formic acid, LC-MS grade, Merck, Darmstadt, Germany). The flow rate at 0.4 mL/min throughout the 25 min gradient. The chromatographic gradient was set as follows: linear gradient of 5–65% B over 20 min, the gradient was ramped to 90% B in 3 min (20–23 min) and held at that composition for 3 min (23–26 min), the composition was returned to 5% B at 26.1 min until 25 min to recondition the column.

The Q-ToF mass spectrometer was operated in data-dependent acquisition (DDA) mode using positive electrospray ionization with the following parameters: interface voltage of 4.0 kV, interface temperature of 300°C, nebulization, and dry gas flow of 3 L/minute, heat block temperature of 400°C, DL temperature of 280°C, detector voltage of 1.8 kV and a flight temperature of 42°C. The spectra, MS1 and MS2, were generated for all ions with an m/z range between 100 and 1200, surpassing an intensity threshold of 3000. Fragmentation of ions was performed using argon as a collision gas at a collision energy of 30 ± 17 eV.

MZmine data pre-processing and GNPS-feature-based molecular networking

The data obtained from the mass spectrometry was converted to an open format, mzML file using MS convert software (<http://proteowizard.sourceforge.net/downloads.shtml>; accessed 02 October 2024). The mass spectrometry data files were first processed using MZmine 3¹⁴. Thereafter, the data was uploaded on the GNPS2-MN (Global Natural Products Social-Molecular Network, Version 28.2) platform (<https://gnps2.org/>) accessed on 06 May 2025, and the data was processed following the Feature-Based Molecular Networking (FBMN) workflow^{15,16}. The data was filtered by removing all MS/MS fragment ions within +/- 17 Da of the precursor m/z and choosing only the top 6 fragment ions in the +/- 50 Da window throughout the spectrum. The precursor ion mass tolerance was set to 0.02 Da, and an MS/MS fragment ion tolerance of 0.02 Da. A network was created where edges were filtered to have a cosine score above 0.7 and more than 6 matched peaks. Further, edges between two nodes were kept in the network only if each node appeared in each other's top 10 most similar nodes. Finally, the maximum size of a molecular family was set to 100, and the lowest-scoring edges were removed from molecular families until the molecular family size was below this threshold. The spectra in the network were then searched against GNPS spectral libraries, which were filtered using the same conditions as described for the spectra above^{15,17}. All retained matches between the network and library spectra were required to score above 0.7 and at least 6 matched peaks. Further annotation of MS/MS spectra was done using the dereplicator¹⁸ and the Sirius platform, Version 5.8.5, using the built-in CSI fingerID and Canopus features^{19–21}. The web interface for feature-based molecular networking (<https://fbmn-statsguide.gnps2.org/>; accessed 06 May 2025) was used to clean up the FBMN data and statistical analysis and integration into the Cytoscape visualization tool²². The molecular networks were visualized using Cytoscape software, Version 3.10.2²³.

Virtual screening of secondary metabolites from *P. rubens*

The X-ray crystal structure of HIV-1 Protease NL4-3 (PDB code: 6PJG) was obtained from the RCSB Protein Data Bank for molecular docking studies. Protein preparation was performed using AutoDock Tools v.1.5.6²⁴, where water molecules, ions, and co-crystallized ligands were removed. Missing side chain atoms and polar hydrogen atoms were added, and Kollman charges were assigned to the protein structure to optimize it for docking. The ligand library was first prepared in 3D format with explicit hydrogens and appropriate protonation states at pH 7.4 using OpenBabel v.2.4.1²⁵. These structures were then processed with Meeko v.0.5.1²⁶ to assign rotatable bonds and convert them to PDBQT format compatible with AutoDock Vina²⁷.

The docking protocol was validated by re-docking the co-crystallized ligand (ORV), with success criteria defined as a root mean square deviation (RMSD) of less than 2.0 Å from the crystallographic pose. The binding site was defined based on the position of the co-crystallized ligand. A two-step docking approach was employed using AutoDock Vina: initial screening was conducted with default parameters (exhaustiveness = 8) to identify promising candidates, followed by a more rigorous docking phase for the top 10% of compounds based on

binding affinity scores, using refined parameters (exhaustiveness=128, number of binding modes=20, and energy range=3 kcal/mol). To ensure reproducibility and adequate sampling of conformational space, each compound was docked in triplicate using different random seeds.

Docking results were ranked according to binding affinity scores, and the top three scoring compounds were selected for subsequent analysis. The ligand binding poses, and protein-ligand interactions were visualized using Discovery Studio Visualizer version 20.1.0.19295²⁸ and PyMol v.3.0²⁹.

Following molecular docking, Density Functional Theory (DFT) calculations were performed using Gaussian 16 software to refine the top-scoring compounds' geometries further. DFT calculations utilized M06-2X functional with the 6-311++G(d, p) basis set for all selected ligands. The geometries of the compounds were optimized to the nearest local minimum, and frequency calculations were performed to confirm that the optimized structures corresponded to true minima. The highest occupied molecular orbital (HOMO) and lowest unoccupied molecular orbital (LUMO) energies, as well as the HOMO-LUMO energy gap (ΔE), were calculated to investigate the electronic properties of the ligands. Additionally, global reactivity descriptors, including chemical potential (μ), chemical hardness (η), softness (S), electrophilic index (ω), and electronegativity (χ) were derived from HOMO-LUMO energies using the following equations:

$$\mu = \frac{E_{HOMO} + E_{LUMO}}{2} \quad (1)$$

$$\eta = \frac{E_{LUMO} - E_{HOMO}}{2} \quad (2)$$

$$S = \frac{1}{\eta} \quad (3)$$

$$\chi = -\mu \quad (4)$$

$$\omega = \frac{\mu^2}{2\eta} \quad (5)$$

Molecular dynamics simulations

Molecular dynamics (MD) simulations were conducted using AMBER 20, employing the FF14SB force field parameters for protein description^{30,31}. The LEAP module was utilized to add hydrogen atoms to the protein and incorporate counter-ions³². The system was enclosed in a TIP3P water box, maintaining a distance of 10 Å between the system surface and the box edge. Periodic boundary conditions were applied, with long-range electrostatics managed using a 12 Å van der Waals cutoff³³. Initial minimization involved a restrained potential of 500 kcal/mol/Å² over 1000 steepest descent steps followed by 1000 conjugate gradient steps on the solute³⁴. This was succeeded by 1000 steps of unrestrained conjugate gradient minimization for the entire system. The system was gradually heated from 0 to 300 K over 1 ps, employing a Langevin thermostat with collision frequency and harmonic restraints set at 5 kcal/mol/Å². An unrestrained equilibration of the system was performed using an NPT ensemble at constant pressure (1 bar) and temperature (300 K)³⁵. The production run for MD simulation lasted 200 ns, utilizing an isothermal-isobaric (NPT) ensemble with a Berendsen barostat³⁶. Coordinates were saved at intervals throughout the simulation, and trajectories were analyzed post-simulation.

Post molecular dynamics simulation analysis

Post-MD trajectory analysis was conducted using AMBER20's PTRAJ and CPPTRAJ modules. Key analyses included root mean square deviation (RMSD) and root mean square fluctuations (RMSF) to assess system stability and flexibility, the radius of gyration (RoG) for compactness, solvent accessible surface area (SASA) to analyze binding site exposure and ligand interactions, and hydrogen bond analysis for insights into interactions.

Binding free energy profiles were calculated using the Molecular Mechanics/Generalized Born Surface Area (MM/GBSA)³⁷⁻³⁹ approach, as follows:

$$\Delta G_{\text{bind}} = G_{\text{complex}} - G_{\text{receptor}} - G_{\text{ligand}} \quad (6)$$

$$\Delta G_{\text{bind}} = E_{\text{gas}} + G_{\text{sol}} - T\Delta S \quad (7)$$

$$E_{\text{gas}} = E_{\text{int}} + E_{\text{vdW}} + E_{\text{ele}} \quad (8)$$

$$G_{\text{sol}} = G_{\text{GB}} + G_{\text{SA}} \quad (9)$$

In these equations, ΔG_{bind} denotes the total binding free energy, E_{gas} indicates gas-phase energy, and G_{sol} represents solvation energy. T and ΔS refer to temperature and solute entropy, respectively. The terms G_{GB} and G_{SA} denote polar and non-polar solvation contributions, while E_{vdW} and E_{ele} specify van der Waals and electrostatic interactions. Residue-wise energy contributions were also calculated to provide insights into the key residues influencing binding affinity.

Results

Secondary metabolite production

The fungal secondary metabolites were produced following a systematic variation of growth media (MEA broth, rice media, oat media) to simulate a one-strain many compounds (OSMAC) approach. The crude extracts were then fractionated using solid phase extraction, which was performed using two mixed-mode reverse-phase

matrices (MAX or MCX) to simplify the extracts. After the solid-phase extraction, the MEA crude extract partially purified using the MAX cartridge resulted in four fractions: MEA MAX crude extracts (0,004 g), MEA MAX 5% (0,003 g), MEA MAX 45% (0,003 g) and MEA MAX 95% (0,002 g). The MCX cartridge also resulted in MEA MCX 5% (0,001 g), MEA MCX 45% (0,001 g) and MEA MCX 95% (0,001 g) fractions. The oats crude extract purified using the MAX cartridge resulted in four fractions: oats MAX crude extracts (0,001 g), oats MAX 5% (0,001 g), oats MAX 45% (0,002 g) and oats MAX 95% (0,002 g). The MCX cartridge gave rise to four fractions: oats MCX crude extracts (0,001 g), oats MCX 5% (0,001 g), oats MCX 45% (0,001 g), oats MCX 95% (0,002 g). Rice crude extracts purified using the MAX cartridge resulted in four fractions: rice MAX crude extracts (0,001 g), rice MAX 5% (0,002 g), rice MAX 45% (0,001 g), and rice MAX 95% (0,001 g). On the other end, the MCX cartridge resulted in four fractions: rice MCX crude extracts (0,001 g), rice MCX 5% (0,001 g), rice MCX 45% (0,002 g), rice MCX 95% (0,002 g).

Luciferase-based antiviral activity assay

The anti-HIV-1 activities of the crude extracts and fractions from *P. rubens* P03MB2 were assessed using a luciferase-based antiviral reporter gene assay on the TZM-bl cell line. Antiviral activity was measured by calculating the percentage of viral inhibition of the extracts at varying 3-fold dilutions, and the results were reported as dose-response curves (Figs. 1, 2, 3, 4, 5 and 6). The pharmacological efficacy and potency of the extracts in this study were assessed relative to the control AZT. As expected, AZT demonstrated a strong pharmacological effect (high efficacy).

All the MEA MAX fractions exhibited weak efficacy (<90% HIV inhibition). However, the crude extract and the 5% fraction displayed greater potency than AZT (0.002407 $\mu\text{g}/\text{mL}$), with values of 0.0008991 $\mu\text{g}/\text{mL}$ (~0.27-fold) and 0.001445 $\mu\text{g}/\text{mL}$ (~1.66-fold), respectively (Fig. 1). For the MEA MCX fractions, only the 5% fraction exhibited enhanced efficacy, achieving 97.5% HIV inhibition. Meanwhile, only the 95% fraction displayed promising potency (0.2810 $\mu\text{g}/\text{mL}$, Fig. 2). In the Oats MAX fractions, the 45% and 95% fractions showed enhanced efficacy (91% HIV inhibition). However, only the 45% fraction exhibited promising potency (0.7063 $\mu\text{g}/\text{mL}$, Fig. 3). Similarly, in the Oats MCX group, the 5% and 45% fractions demonstrated strong pharmacological effects, with 96.5% and 95.5% HIV inhibition, respectively. The 95% fraction stood out with a 0.0001169 $\mu\text{g}/\text{mL}$ potency, which is more significant than that of AZT (0.002407 $\mu\text{g}/\text{mL}$). Other Oats MCX fractions also exhibited promising potency (0.02–0.04 $\mu\text{g}/\text{mL}$, Fig. 4). For the rice extracts, the 45% and 95% fractions demonstrated strong pharmacological effects, with 101% and 99% HIV inhibition, respectively (Fig. 5). The rice MAX crude extract (0.009807 $\mu\text{g}/\text{mL}$) and the 45% fraction (0.08032 $\mu\text{g}/\text{mL}$) exhibited notable potency.

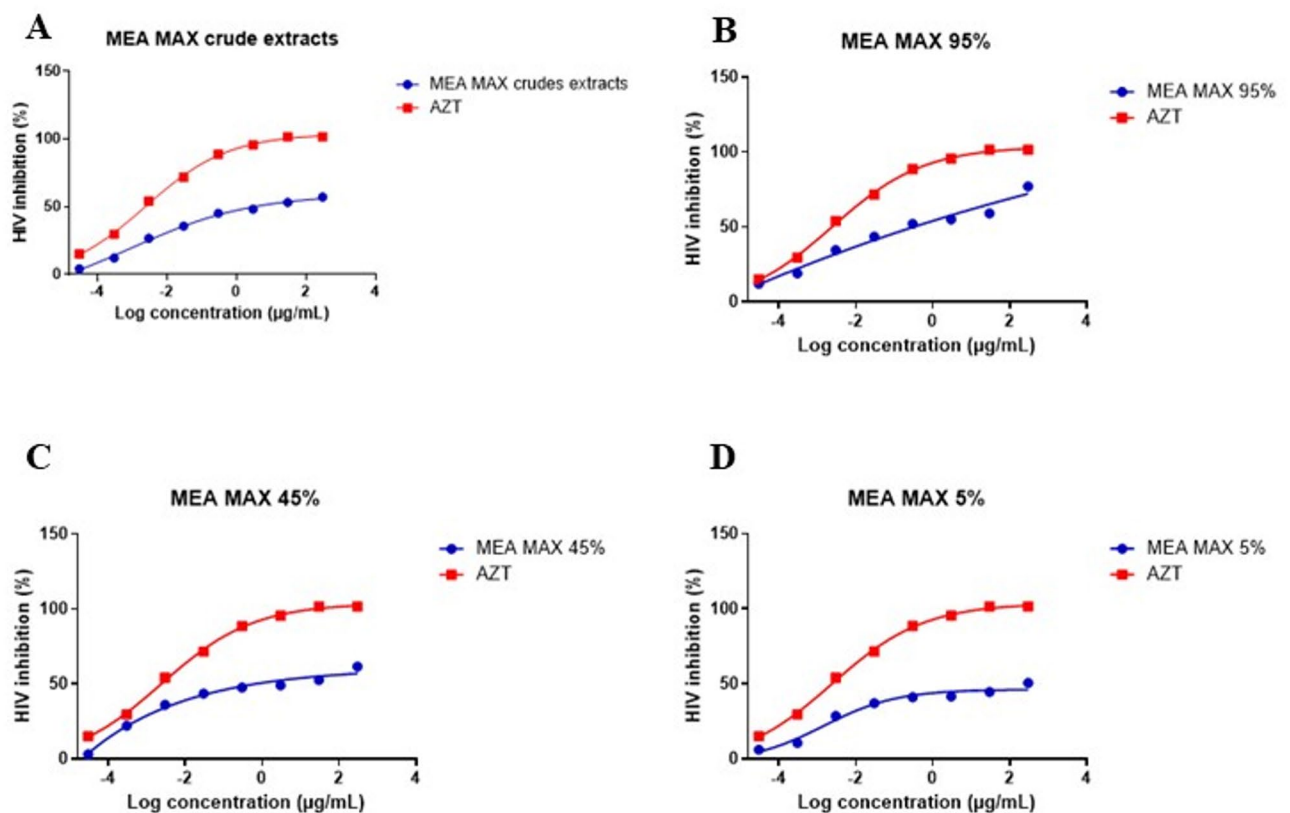


Fig. 1. Dose-response curve of MEA media MAX crude extract's anti-HIV activity tested in TZM-BI cells for MEA media eluted in MAX cartridges. AZT was used as a positive control. MEA MAX crude extract (A), MEA MAX 95% fraction (B), MEA MAX 45% fraction (C) and MEA MAX 5% fraction (D).

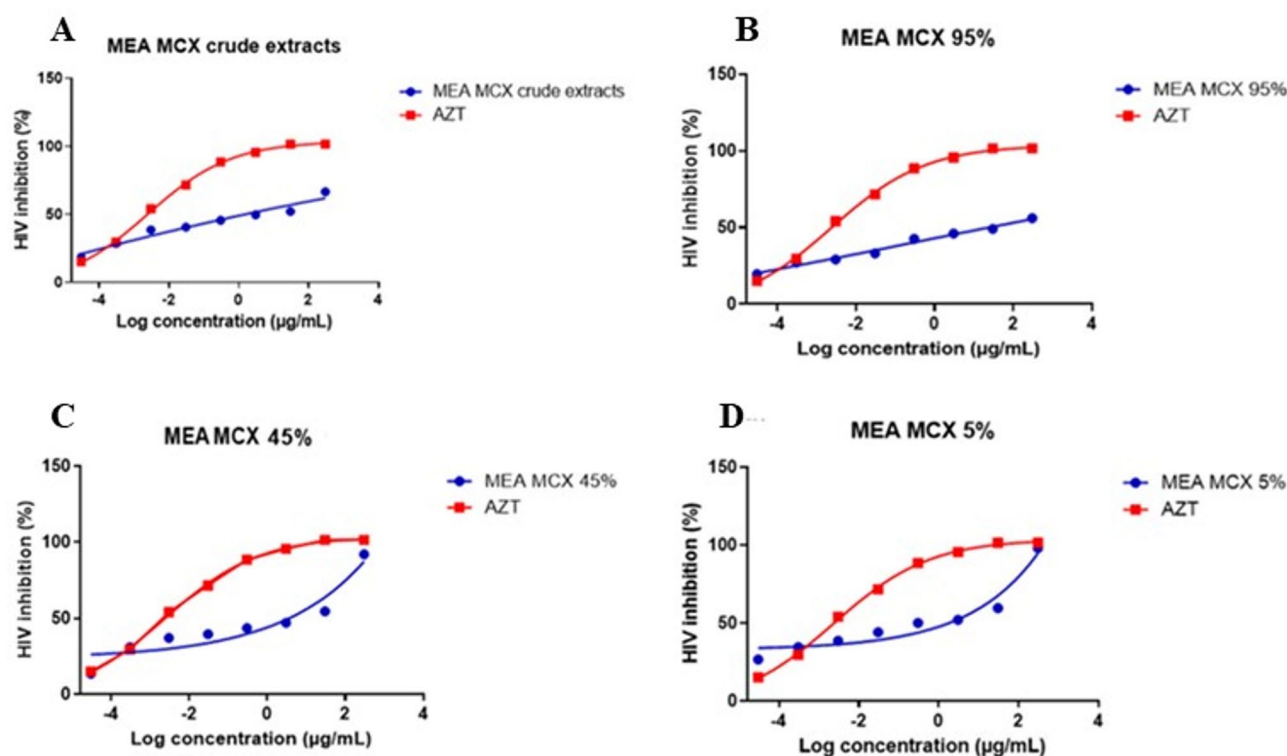


Fig. 2. Dose-response curve of MEA MCX crude extract's anti-HIV activity tested in TZM-B1 cells for MEA media eluted in MCX cartridges. AZT was used as a positive control. MEA MCX crude extracts (A), MEA MCX 95% fraction (B), MEA MCX 45% fraction (C) and MEA 5% fraction (D).

All rice MCX fractions displayed high efficacy (98–101% HIV inhibition), although only the 95% fraction showed promising potency (0.08168 µg/mL, Fig. 6). The HIV inhibition (pharmacological effects or efficacy) and potency (IC_{50}) results for *Penicillium rubens* P03MB2 extracts are summarized in Table 1 (MEA media), Table 2 (Oat media), and Table 3 (Rice media), respectively.

Feature-based molecular network analysis

Nine fractions and three media controls (MEA, rice, and oat) were selected for LC-HRMS/MS analysis. These included two fractions from MEA (MEA_MCX 5% and MEA_MCX 95%), four fractions from rice media (Rice_MCX 5%, Rice_MCX 45%, Rice_MCX 95% and Rice_MAX 45%), and three fractions from oats media (Oats_MCX 5%, Oats_MCX 45%, and Oats_MCX 95%). Spectral analysis was performed using a feature-based molecular network (FBMN) to obtain a global view of the chemical space in *P. rubens* P03MB2 under various nutrient conditions and to facilitate metabolite annotation and dereplication. The constructed FBMN-molecular network comprised 6358 node clusters into 705 molecular families with 42 annotated nodes. FBMN data cleaning and statistical analysis were performed to identify true features and remove blanks before this was embedded into the Cytoscape visualization tool. After removing blanks, the final network consisted of true features arranged into 3576 nodes with 40 annotated nodes (Fig. 7).

Virtual screening and molecular interaction analysis

The molecular docking approach was validated through an RMSD analysis, with the re-docked pose of ORV showing an RMSD value of 0.81 Å compared to its experimentally co-crystallized orientation. Following DFT geometry optimization, frequency calculations confirmed the absence of imaginary frequencies in the optimized geometries, ensuring our computational models' structural stability and reliability. The electronic properties of the compounds revealed nuanced differences in molecular stability and reactivity (Table 4).

Diosgenin exhibited the largest energy gap ($\Delta E=7.60$ eV), which indicates minimal reactivity and high kinetic stability. In contrast, cyclopiazonic acid displayed the smallest energy gap ($\Delta E=6.25$ eV), suggesting higher reactivity. Aflatoxin B1 displayed the most negative chemical potential ($\mu=-4.69$ eV), reflecting a strong electron-withdrawing capacity, while its highest electrophilicity index ($\omega=3.41$) indicates a strong tendency to accept electrons. ORV and diosgenin exhibited moderate electrophilicity ($\omega=2.42$ and $\omega=2.11$, respectively), with ORV showing balanced stability and reactivity. These findings highlight aflatoxin B1's electrophilic nature and diosgenin's superior stability, which could influence its binding characteristics and efficacy as an inhibitor.

Complementing the electronic property analysis, we evaluated key physicochemical properties and molecular docking interactions (Table 5). The physicochemical properties of the studied compounds revealed variations that may influence their potential as HIV-1 protease inhibitors. Diosgenin, with the highest molecular

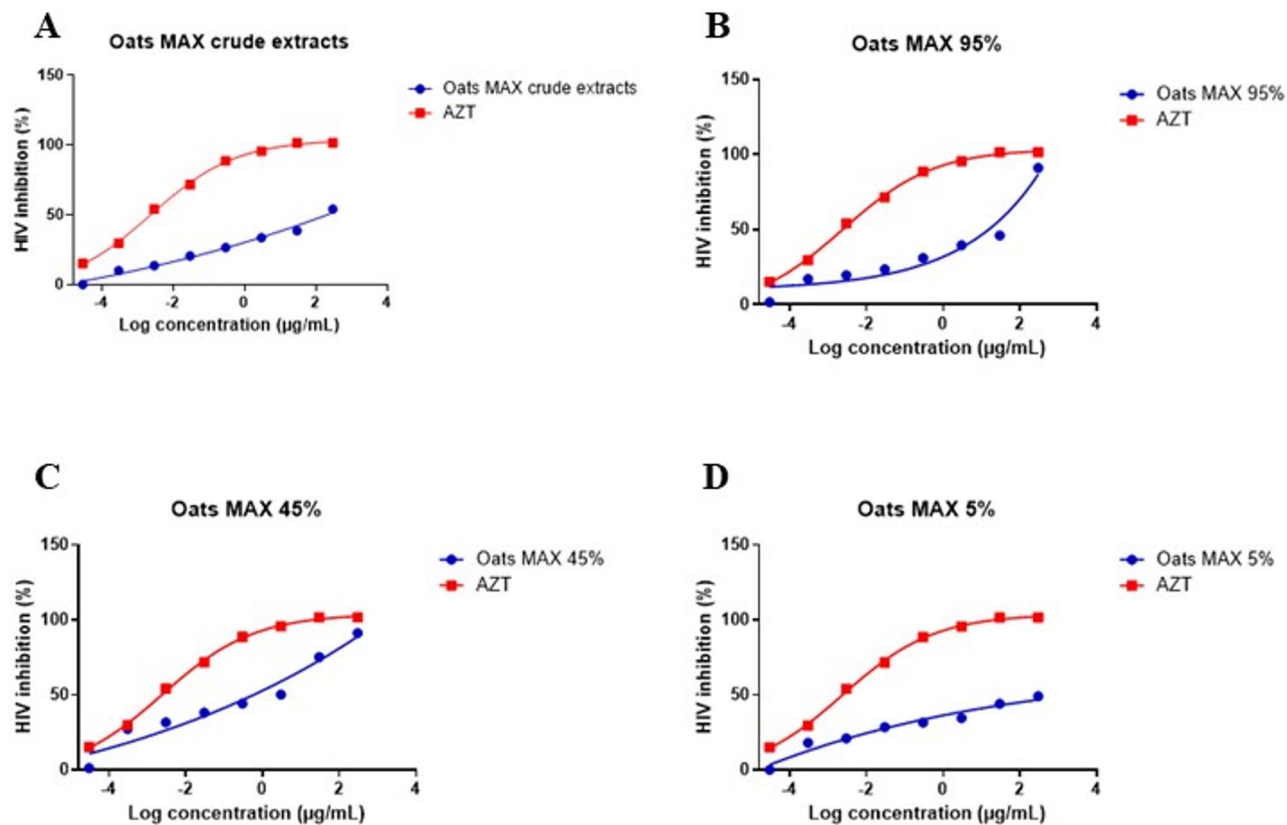


Fig. 3. Dose-response curve of *Penicillium rubens* extract's anti-HIV activity tested in TZM-B1 cells for Oats media eluted in MAX cartridges. AZT was used as a positive control. Oats MAX crude extracts (A), Oats MAX 95% fraction (B), Oats MAX 45% fraction (C) and Oats MAX 5% fraction (D).

weight (414.63 Da) and lipophilicity ($\text{LogP}=5.72$), suggests enhanced membrane permeability. In contrast, aflatoxin B1, with the lowest molecular weight (312.28 Da) and lower lipophilicity ($\text{LogP}=2.28$), may have reduced cellular penetration. Notable differences in topological polar surface area (TPSA) were observed, with aflatoxin B1 and cyclopiazonic acid exhibiting higher TPSA values (74.97 and 73.40 Å², respectively), which could impact solubility and transport. Additionally, ORV's high number of hydrogen bond acceptors (8) and rotatable bonds (4) suggests significant molecular flexibility, potentially enhancing its interaction capabilities. Diosgenin demonstrated the strongest binding affinity with a docking score of -8.8 kcal/mol. Cyclopiazonic acid followed with a docking score of -7.9 kcal/mol, while aflatoxin B1 showed a binding affinity of -7.8 kcal/mol. ORV, characterized by moderate electrophilicity ($\omega=2.42$), displayed a comparatively lower binding affinity of -6.8 kcal/mol.

Detailed molecular interaction analyses revealed distinct binding patterns within the enzyme's active site for each inhibitor. Diosgenin (Fig. 8A) formed a dense network of interactions characterized by van der Waals contacts with residues LEU A:23, LEU B:23, ASP B:25, ALA A:28, GLY A:48, GLY A:49, and additional stabilizing interactions through hydrogen bonds with ARG B:8, ASP A:25, and GLY B:27. Carbon-hydrogen bonds with GLY A:27 and GLY A:49 further stabilized diosgenin's position within the hydrophobic pocket. Additionally, alkyl and π -alkyl interactions involving ILE A:50, ILE B:50, ALA A:28, PRO B:81, and VAL B:82 also contributed to the stabilization of the ligand within the active site, indicating a high affinity for HIV-1 protease. Cyclopiazonic acid (Fig. 8B) exhibited multiple interactions within the active site, forming key van der Waals contacts with ARG A:8, LEU A:23, ILE A:84, ILE B:47, LYS B:45, ASP B:29, ASP B:30, ILE B:50, and MET B:46 in the hydrophobic region. Conventional hydrogen bonds formed with GLY B:27 complemented by carbon-hydrogen bonds with GLY B:48 enhanced its binding stability through alkyl and π -alkyl interactions with VAL A:82, PRO A:81, and PHE B:53.

Aflatoxin B1 (Fig. 9A) demonstrated significant binding through van der Waals interactions with LEU A:23, ILE A:84, ILE B:84, GLY A:49, GLY B:27, ASP B:30, and GLY B:49 in the hydrophobic pocket. It formed conventional hydrogen bonds with ARG A:8 and ILE B:50, while benefiting from alkyl and π -alkyl interactions involving VAL A:82, ILE A:50, ALA B:28, VAL B:32, and ILE B:47 to enhance binding stability. The control ligand ORV (Fig. 9B) displayed comprehensive interactions characterized by van der Waals contacts with LEU A:23, LEU B:23, ALA B:28, ASP B:30, VAL B:32, and ILE B:84 in hydrophobic regions. Extensive hydrogen bonding was observed with ASP A:25, GLY A:27, ASP B:25 as well as carbon-hydrogen bonds involving GLY B:49 and other residues like ALA A/B28 and ILE B:84 further secured its position within the active site through additional alkyl and π -alkyl interactions.

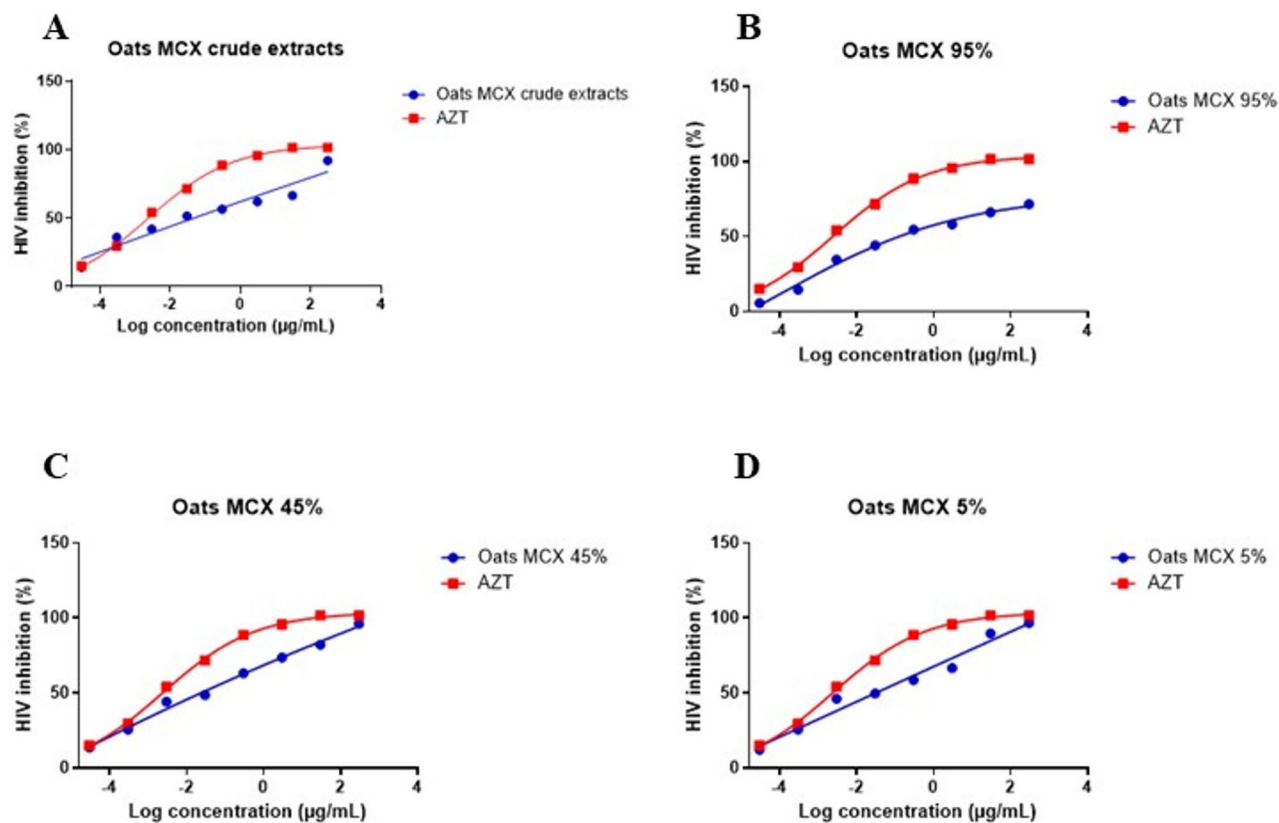


Fig. 4. Dose-response curve of *Penicillium rubens* extract's anti-HIV activity tested in TZM-BI cells for Oats media eluted in MCX cartridges. AZT was used as a positive control. Oats MCX crude extracts (A), Oats MCX 95% fraction (B), Oats MCX 45% fraction (C) and Oats MCX 5% fraction (D).

Post-MD analysis evaluated the stability and dynamics of protein-ligand interactions across all complexes. Multiple parameters were analysed to assess binding stability and conformational changes comprehensively. RMSD analysis of the protein backbone and ligand positions revealed distinct stability profiles among the complexes (Fig. 10A). All systems achieved equilibrium after approximately 50 ns, with diosgenin demonstrating superior conformational stability (1.16 Å). Cyclopiazonic acid also maintained stable binding with RMSD fluctuations reaching 1.33 Å. In contrast, aflatoxin B1 and ORV showed higher conformational mobility, with RMSD values of 1.54 Å and 1.55 Å, respectively, suggesting less stable binding interactions. Local flexibility assessment through RMSF analysis highlighted significant differences in residue mobility (Fig. 10B). The catalytic regions, particularly around residues Asp25 and Ile50, showed minimal fluctuations in diosgenin (0.86 Å) and cyclopiazonic acid (0.88 Å) complexes. Aflatoxin B1 and ORV exhibited higher residue mobility (RMSF 0.99 Å and 0.90 Å, respectively), indicating reduced binding stability. Protein compactness, monitored through RoG, revealed differential structural behaviour (Fig. 11A). Diosgenin and aflatoxin B1 maintained more compact conformations, with RoG values of 8.47 Å and 7.79 Å, respectively, while cyclopiazonic acid and ORV exhibited slight structural expansion, with RoG values of 9.45 Å and 9.14 Å, respectively.

SASA measurements indicated varying degrees of solvent exposure among the complexes (Fig. 11B). Diosgenin exhibited a SASA value of approximately 741 Å², cyclopiazonic acid showed a SASA value of around 979 Å², ORV had a SASA value of about 420 Å², and aflatoxin B1 displayed a SASA value of approximately 572 Å². The lower SASA values for ORV and aflatoxin B1 suggest better burial within the binding pocket than diosgenin and cyclopiazonic acid. Hydrogen bond analysis provided further insights into binding stability (Fig. 12A). Aflatoxin B1 formed the most stable hydrogen bonding network, with an average of 4.46 hydrogen bonds throughout the simulation, followed by diosgenin with approximately 2.93 bonds and cyclopiazonic acid with around 2.08 bonds. ORV formed the fewest hydrogen bonds, averaging 1.57 bonds, which may correlate with its relatively lower binding stability.

Principal component analysis (PCA) revealed distinct conformational sampling patterns (Fig. 12B). Aflatoxin B1 exhibited the most expansive conformational space, with standard deviations of ± 7.2986 in PC1 and ± 5.8549 in PC2, indicating significant structural variability and flexibility. Cyclopiazonic acid showed moderate conformational variability, with standard deviations of ± 6.4744 in PC1 and ± 3.7219 in PC2, suggesting some adaptability while maintaining a relatively compact distribution. Diosgenin presented the most constrained conformational exploration, with the lowest standard deviations of ± 4.5341 in PC1 and ± 4.2117 in PC2. This suggests a more rigid molecular structure with tightly controlled dynamics that may lead to more predictable binding characteristics. ORV displayed substantial conformational dispersion with standard deviations of

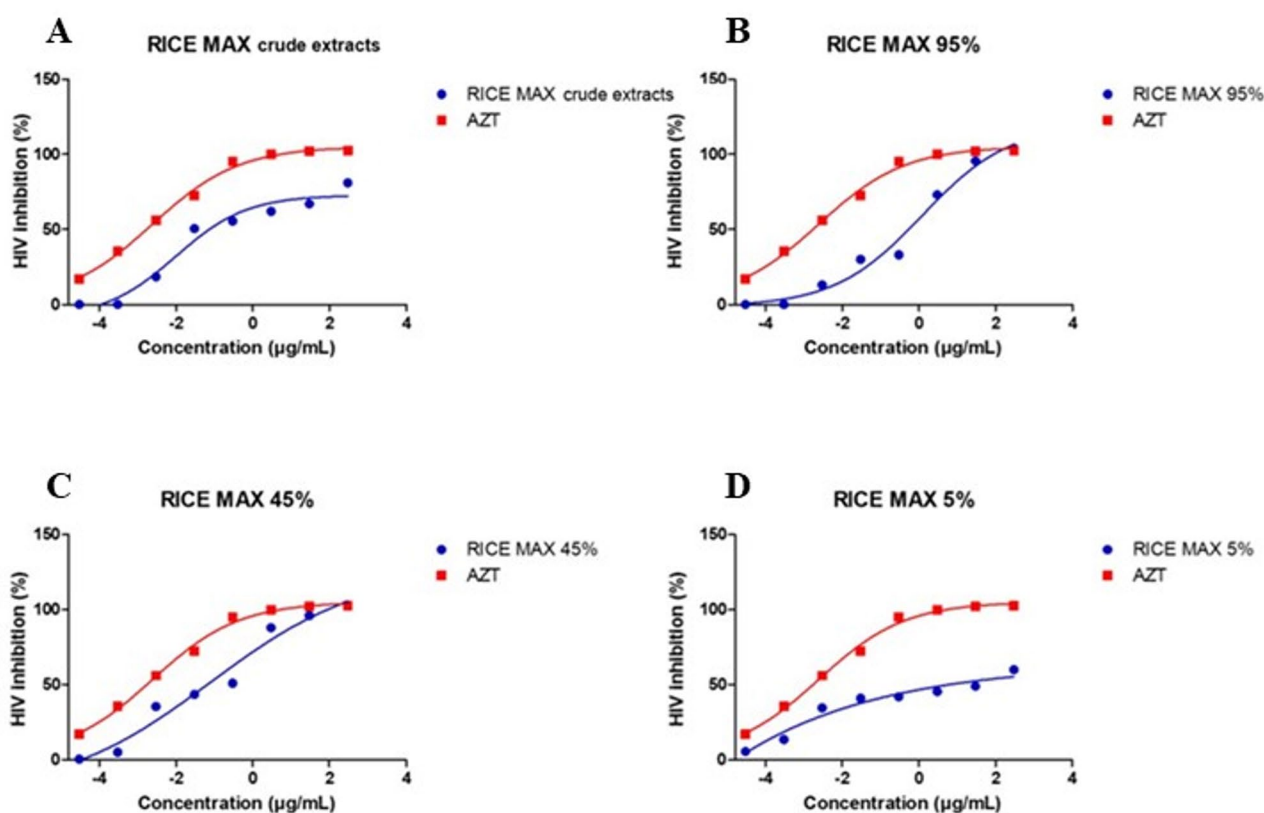


Fig. 5. Dose-response curve of *Penicillium rubens* extract's anti-HIV activity tested in TZM-B1 cells for Rice media eluted in MAX cartridges. AZT was used as a positive control. Rice MAX crude extracts (A), Rice MAX 95% fraction (B), Rice MAX 45% fraction (C) and Rice MAX 5% fraction (D).

± 6.5256 in PC1 and ± 4.2574 in PC2, indicating notable structural fluctuations contributing to its complex molecular dynamics. The pairwise cluster centre distances further illuminated these differences, with the smallest distance of 0.0390 observed between Aflatoxin B1 and ORV, and the largest distance of 0.0722 between Aflatoxin B1 and Diosgenin. These variations in conformational sampling suggest differing degrees of molecular adaptability among the compounds.

The binding free energies for each HIV-1 protease-inhibitor complex were computed using the MM/GBSA approach, with the results summarized in (Table 6). ORV demonstrated the most favourable binding free energy ($\Delta G_{\text{bind}} = -47.75 \pm 0.12$ kcal/mol), primarily driven by strong van der Waals interactions ($\Delta E_{\text{vdw}} = -56.85 \pm 0.11$ kcal/mol) and nonpolar solvation energies ($\Delta G_{\text{nonpol}} = -7.84 \pm 0.01$ kcal/mol). This suggests that ORV forms robust hydrophobic interactions with HIV-1 protease, substantially contributing to its potential inhibitory mechanism. Diosgenin also exhibited a favourable binding free energy ($\Delta G_{\text{bind}} = -34.59 \pm 0.11$ kcal/mol), characterized by substantial van der Waals interactions ($\Delta E_{\text{vdw}} = -40.67 \pm 0.12$ kcal/mol). These hydrophobic interactions indicate a significant molecular recognition mechanism between diosgenin and the protease active site.

In contrast, cyclopiazonic acid ($\Delta G_{\text{bind}} = -29.30 \pm 0.44$ kcal/mol) showed a distinctive binding profile with a notable contribution from electrostatic interactions ($\Delta E_{\text{ele}} = -9.52 \pm 0.39$ kcal/mol), which was counterbalanced by a higher polar solvation energy ($\Delta G_{\text{pol}} = 21.03 \pm 0.23$ kcal/mol). The unfavourable polar solvation energy suggests that cyclopiazonic acid may experience less favourable interactions with the solvent, impacting its overall binding efficiency. Aflatoxin B1 displayed the least favourable binding energy ($\Delta G_{\text{bind}} = -25.66 \pm 0.21$ kcal/mol), with relatively weaker contributions from van der Waals and electrostatic interactions. This suggests a comparatively less stable interaction with the HIV-1 protease.

Interaction energy decomposition analysis was performed further to elucidate each inhibitor's contributions to binding affinity. The detailed analysis revealed distinct molecular interaction patterns across the studied compounds. Diosgenin exhibited a distinctive binding profile characterized by prominent van der Waals interactions (Fig. 13A). ARG B:8 ($\Delta G_{\text{total}} = -1.213$ kcal/mol) and PRO B:81 ($\Delta G_{\text{total}} = -1.305$ kcal/mol) were key contributors, suggesting effective molecular packing within the binding pocket. Additional stability was derived from electrostatic and non-polar solvation effects, particularly from hydrophobic residues such as ILE 50 ($\Delta G_{\text{total}} = -1.243$ kcal/mol) and LEU B:23 ($\Delta G_{\text{total}} = -1.418$ kcal/mol). ORV's binding was predominantly characterized by significant van der Waals interactions, with key hydrophobic residues playing critical stabilization roles (Fig. 13B). Notably, ILE B:50 ($\Delta G_{\text{total}} = -2.184$ kcal/mol) and PRO A:81 ($\Delta G_{\text{total}} = -1.106$ kcal/mol) emerged as pivotal residues, establishing strong hydrophobic interactions. Complementary hydrophobic residues such as VAL A:82

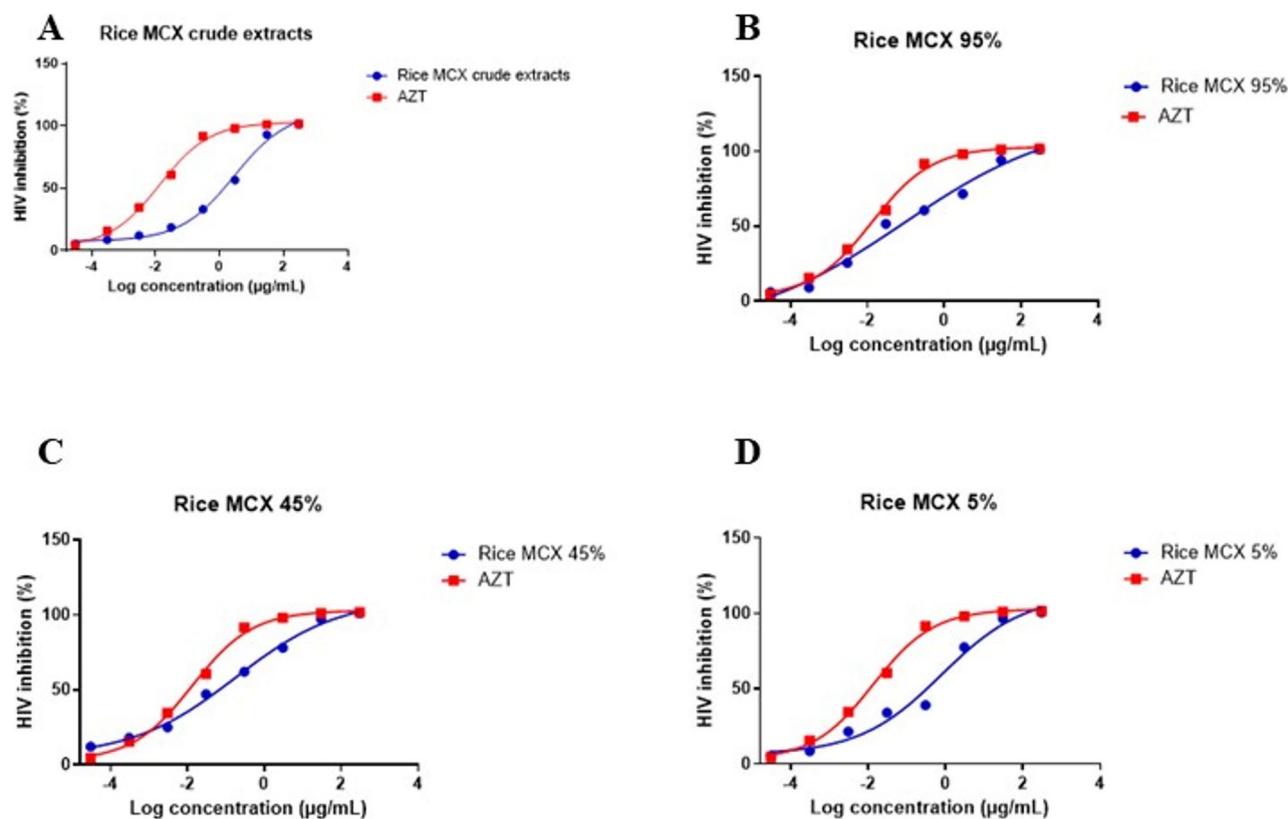


Fig. 6. Dose-response curve of *Penicillium rubens* extract's anti-HIV activity tested on TZM-B1 cells for Rice media eluted in MCX cartridges. AZT was used as a positive control. Rice MCX crude extracts (A), Rice MCX 95% fraction (B), Rice MCX 45% fraction (C) and Rice MCX 5% fraction (D).

<i>Penicillium rubens</i> P03MB2 fractions (MEA media)	IC ₅₀ (µg/mL)	HIV inhibition %
MEA MAX crude extracts	0,0008991	64,5
MEA MAX 5%	0,001445	65
MEA MAX 45%	1,21338	79,5
MEA MAX 95%	3,40401	87
MEA MCX crude extracts	1,2971	54
MEA MCX 5%	3.583e + 013	97,5
MEA MCX 45%	5.950e + 016	88
MEA MCX 95%	0,2810	36
AZT	0,002407	101

Table 1. HIV-1 Inhibition concentration (IC₅₀) on TZM-B1 cells for *Penicillium Rubens* P03MB2 extracts obtained from MEA media. *Eluted in 5%, 45%, and 95% methanol.

and ILE A:84 further enhanced binding stability, underscoring the prominence of hydrophobic interactions in ORV's binding mechanism.

Similarly, aflatoxin B1 demonstrated a complex interplay between van der Waals and electrostatic interactions. ARG A:8 ($\Delta G_{\text{total}} = -2.386$ kcal/mol) stood out as a key contributor, combining favourable van der Waals and electrostatic terms (Fig. 14A). GLY A:27 ($\Delta G_{\text{total}} = -1.559$ kcal/mol) also significantly stabilises the ligand-receptor complex, suggesting that hydrophobic and electrostatic interactions were crucial for aflatoxin's binding affinity. Hydrophobic residues predominantly drove the binding of cyclopiazonic acid. ILE A:50 ($\Delta G_{\text{total}} = -1.243$ kcal/mol) and VAL B:82 ($\Delta G_{\text{total}} = -1.233$ kcal/mol) underscored the importance of hydrophobic interactions in enhancing binding stability (Fig. 14B). Interestingly, polar residues like ASP A:29 ($\Delta G_{\text{total}} = 0.582$ kcal/mol) contributed positively, indicating that polar solvation effects may modulate the overall binding dynamics.

Penicillium rubens P03MB2 fractions (Oats media)	IC ₅₀ (µg/mL)	HIV inhibition %
Oats MAX crude extracts	158,4893	54
Oats MAX 5%	Not converged	49
Oats MAX 45%	0,7063	91
Oats MAX 95%	3.843e + 015	91
Oats MCX crude extracts	0,0446	88,5
Oats MCX 5%	0,0316	96,5
Oats MCX 45%	0,0208	95,5
Oats MCX 95%	0,0001169	71,5
AZT	0,002407	101

Table 2. HIV-1 Inhibition concentration (IC₅₀) on TZM-BL cells for *Penicillium Rubens* P03MB2 extracts obtained from oat media. *Eluted in 5%, 45%, and 95% methanol; not converged (no sigmoid shape), could not determine IC₅₀.

Penicillium rubens P03MB2 fractions Rice	IC ₅₀ (µg/mL)	HIV inhibition %
Rice MAX crude extracts	0,009807	76
Rice MAX 5%	3,3419	68
Rice MAX 45%	0,08032	99
Rice MAX 95%	1,203	101
Rice crude extract MCX	2,841	100
Rice MCX 5%	0,7883	98
Rice MCX 45%	0,1795	98
Rice MCX 95%	0,08168	101
AZT	0,002407	101

Table 3. HIV-1 Inhibition concentration (IC₅₀) on TZM-BL cells for *Penicillium Rubens* P03MB2 extracts obtained from rice media. *Eluted in 5%, 45%, and 95% methanol.

Discussion

The *P. rubens* P03MB2 complex crude extracts and fractions were analyzed for anti-HIV-1 activity using the luciferase reporter gene assay. The MEA crude extract and 5% MAX fraction showed higher inhibition of HIV-1 virus with 2.67 and 1.66-fold more than the AZT control (0.00241 µg/mL), respectively. The most notable antiviral activity in oats fractions was observed in the MCX 95% fraction, which exhibited an IC₅₀ value of 0,0001169 µg/mL, 21-fold higher than that of the positive reference AZT. Two fractions of rice (crude extracts and MAX 45% fractions) had good anti-HIV-1 activity profiles, reaching IC₅₀ of 0.00981 and 0.08032 µg/mL, respectively. In the MCX fraction of oats media and rice media, we noted that antiviral activity (IC₅₀) increased proportionally with the increasing strength of methanol used to elute the fraction. Increased strength of an organic solvent, such as methanol, has been shown to result in a higher yield in the extraction of secondary metabolites⁴⁰. Although all media evaluated in this study produced extracts with anti-HIV-1 activity, good activity was observed from oats media.

We further conducted an untargeted metabolomics analysis followed by a feature-based molecular networking. Molecular networking resulted in 3576 metabolites with 40 annotated compounds, revealing that only 1.1% of compounds were known from this analysis. Only 24 of the annotated compounds were secondary metabolites produced from the fungal extracts. Most fungal secondary metabolites are produced from non-canonical biosynthetic pathways, making their prediction using bioinformatics pipelines challenging. Based on this fact, the low annotation observed in this study is not surprising. To prioritize compounds with potential anti-HIV-1 activity, we adopted an in silico approach to analyse the binding efficiencies of identified compounds from MS spectra to an HIV protease enzyme using molecular docking. Compounds including diosgenin, alphacyclopiazonic acid, alternariol, daidzein and aflatoxin showed a docking score between -7 and -8.8 kcal/mol. Most of these compounds are known to be mycotoxins produced by different fungal species.

Cyclopiazonic acid (CPA) exhibited a binding affinity of -7.9 kcal/mol with a moderate energy gap ($\Delta E = 6.25$ eV) and balanced electronic properties ($\omega = 2.36$). It also showed to engage in stable van der Waals and π -alkyl interactions with key residues such as ARG A:8 and PRO A:81. CPA is an indole alkaloid produced by certain fungal species, including those from the genera *Aspergillus* and *Penicillium*⁴¹. CPA was produced abundantly in oats MCX 95%, corroborating the higher potency observed in the oats MCX 95% fraction. CPA has been shown in previous docking studies to exhibit antiviral activity against HIV protease (-7.9 kcal/mol), COVID-19 (-6.61 kcal/mol⁴² and human respiratory syncytial virus (RSV). In other studies, it was shown to inhibit calcium ATPase in the endoplasmic reticulum, thereby increasing intracellular calcium in Hep2 cells⁴³. Time of addition assays conducted in a study by Cui et al.⁴⁴ showed that it inhibits the viral genome replication and transcription steps. Therefore, one can deduce that the inhibition mechanism occurs through increased intracellular calcium

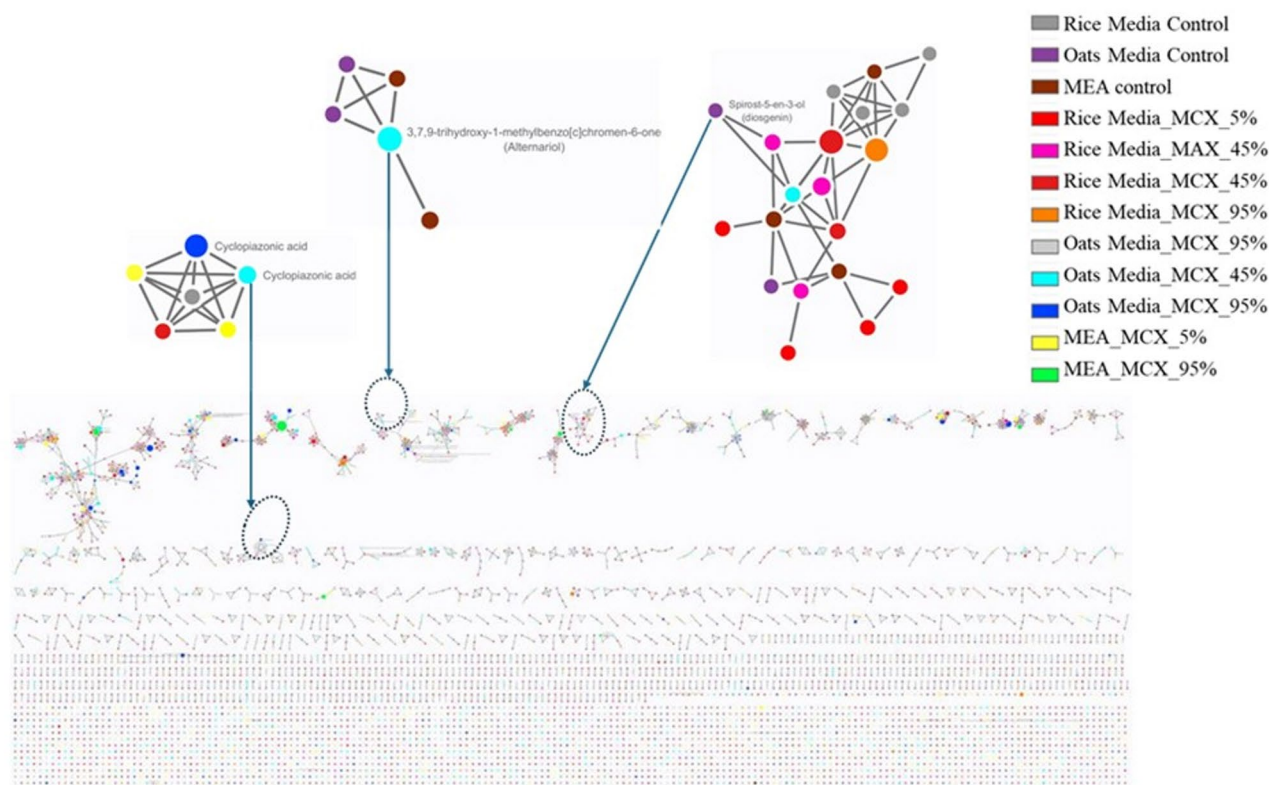


Fig. 7. Feature-based molecular network of *P. rubens* P03MB2. The color of each node corresponds to the compound media used to produce the extract.

Compounds	<i>EHOMO</i>	<i>ELUMO</i>	ΔE	μ	ρ	χ	<i>s</i>	ω
Aflatoxin B1	-7.92	-1.46	6.46	-4.69	3.23	4.69	0.31	3.41
Cyclopiazonic acid	-6.97	-0.72	6.25	-3.84	3.12	3.84	0.32	2.36
Diosgenin	-7.82	-0.21	7.60	-4.01	3.80	4.01	0.26	2.11
ORV	-7.47	-0.65	6.83	-4.06	3.41	4.06	0.29	2.42

Table 4. Orbital energies of the identified compounds.

Ligand	MW	LogP	TPSA (\AA^2)	HBD	HBA	RB	Binding Affinity (kcal/mol)
Diosgenin	414.63	5.72	38.69	1	3	1	-8.8
Cyclopiazonic acid	336.39	2.83	73.40	2	3	2	-7.9
Aflatoxin B1	312.28	2.28	74.97	0	6	0	-7.8
ORV (control)	569.66	2.31	14,445	4	8	4	-6.8

Table 5. Virtual screening of the hit compounds against *P. Rubens*. MW - Molecular Weight; HBD - Hydrogen Bond Donors; TPSA - Topological Polar Surface Area; HBA - Hydrogen Bond Acceptors; RB - Rotatable Bonds.

concentration, which is detrimental to viral replication. This might make CPA an interesting lead candidate for chemical modification since it presents a unique antiviral mechanism based on increasing intracellular calcium concentration in cells.

Another interesting molecule was diosgenin (spirost-5-en-3-ol), also identified in oats media fractions (MCX 45% and 95%). We observed that diosgenin had a significant binding affinity (-8.8 kcal/mol) and MM-GBSA ΔG score of -50.2 kcal/mol, reflecting its strong binding potential. Diosgenin's large energy gap ($\Delta E = 7.60$ eV) ensures high molecular stability and low reactivity. At the same time, its hydrophobic character (LogP=5.72) and moderate electrophilicity index ($\omega = 2.11$) contribute to robust interactions with the protease's active site.

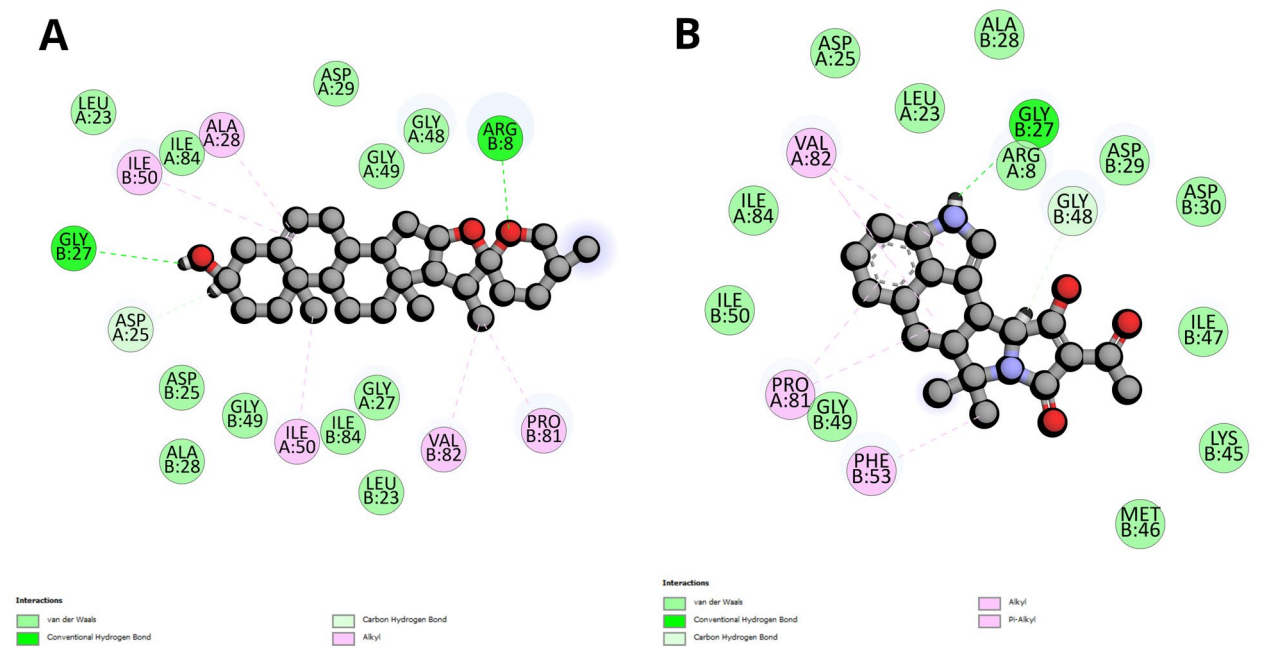


Fig. 8. Molecular docking analysis highlighting key binding interactions and residue contacts for diosgenin (A) and cyclopiazonic acid (B) within the HIV-1 protease active site.

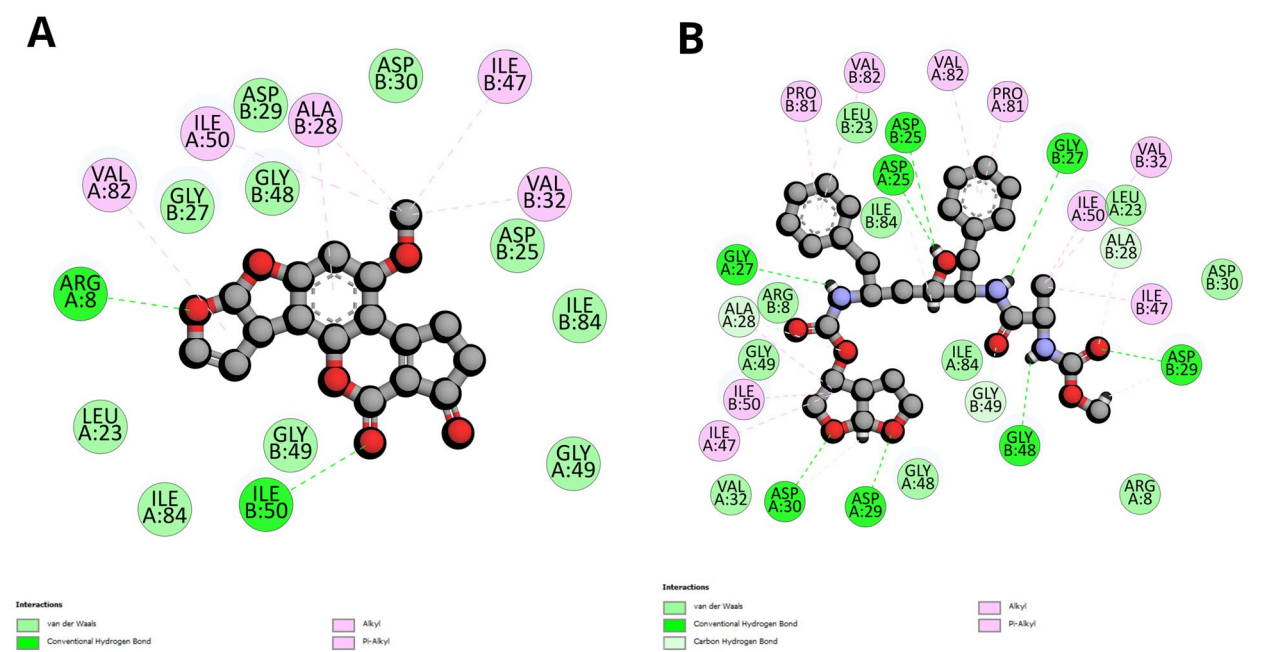


Fig. 9. Molecular docking analysis highlighting key binding interactions and residue contacts for aflatoxin B (A) and ORV (B) within the HIV-1 protease active site.

Notably, diosgenin forms significant van der Waals interactions with LEU A:23 and LEU B:23 and hydrogen bonds with catalytic residues ARG B:8 and ASP A:25. These features allow for reduced molecular flexibility and enhanced stabilization within the active site, marking diosgenin as a standout candidate for further therapeutic exploration.

Diosgenin is a steroidal saponin used in pharmaceuticals as a precursor for steroidal drugs and is mainly found in plants. It is known for its bioactivity properties, including antibacterial, anti-inflammatory, anti-cardiovascular, hypoglycaemic, antioxidant, anticancer, and many other effects⁴⁵. Also, the anti-HIV-1 effect of diosgenin is well documented, with the latest report showing that diosgenin isolated from *Helicteres isora*

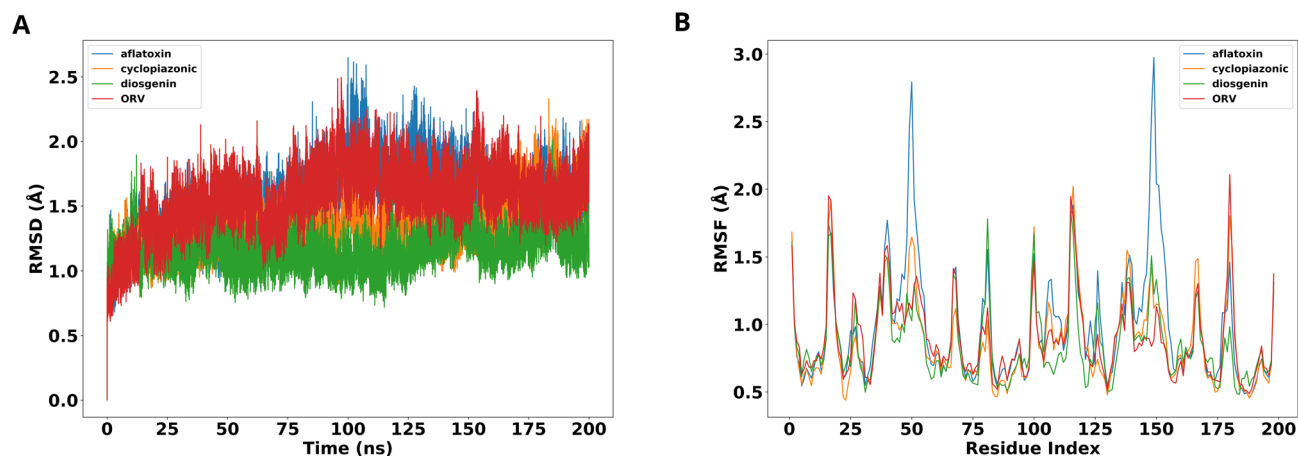


Fig. 10. RMSD (A) and RMSF (B) trajectories of HIV-1 protease complexes with aflatoxin B1, cyclopiiazonic acid, diosgenin, and ORV, illustrating structural stability and flexibility over 200 ns molecular dynamics simulations.

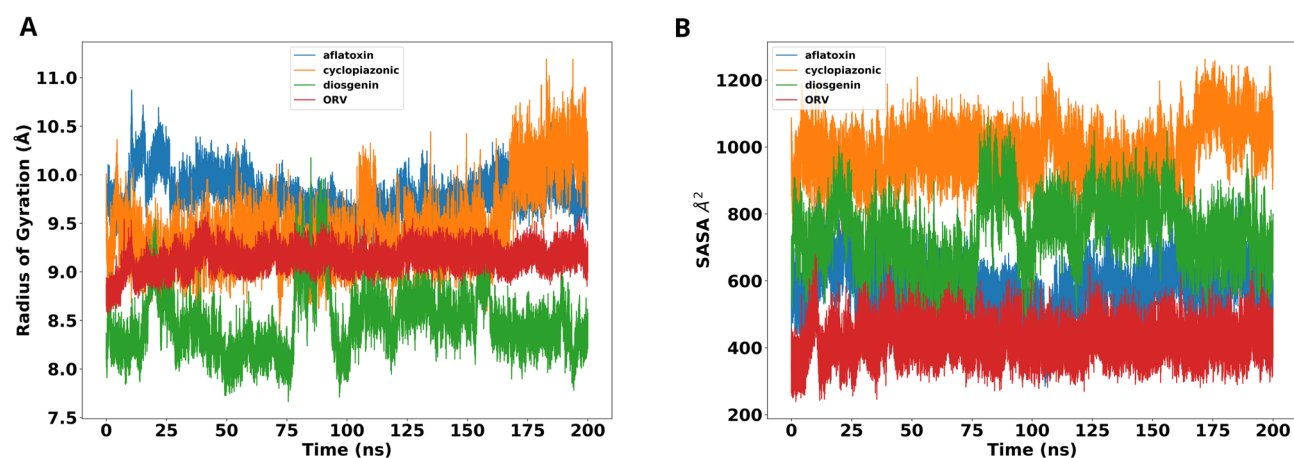


Fig. 11. RoG (A) and SASA (B) trajectories of HIV-1 protease complexes with aflatoxin B1, cyclopiiazonic acid, diosgenin, and ORV, depicting protein compactness and solvent accessibility over 200 ns molecular dynamics simulations.

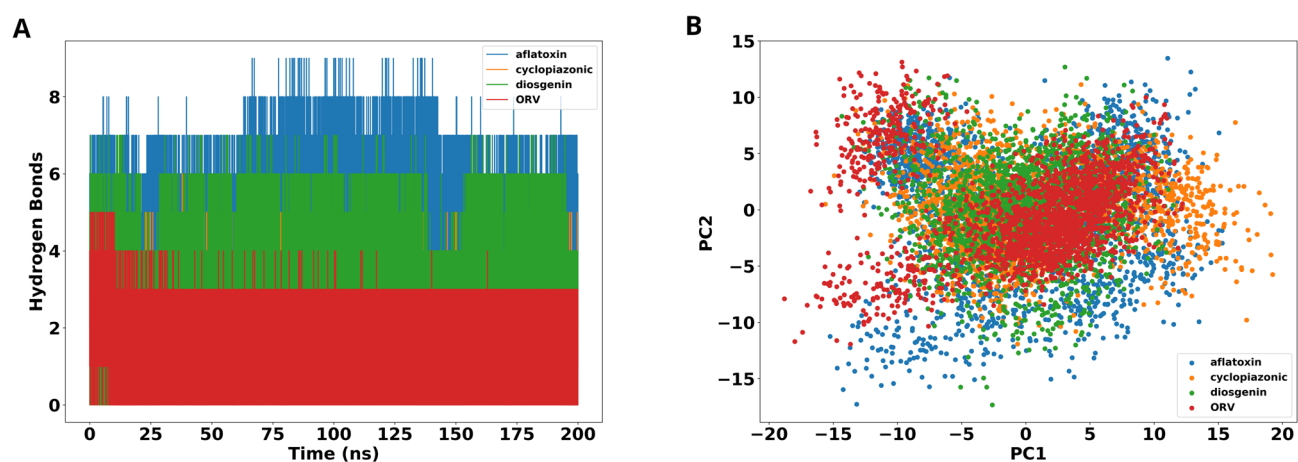


Fig. 12. Hydrogen bond formation (A) and PCA analysis (B) trajectories of HIV-1 protease complexes with aflatoxin B1, cyclopiiazonic acid, diosgenin, and ORV, illustrating binding stability and conformational variance over 200 ns molecular dynamics simulations.

Complexes	ΔG_{bind}	ΔE_{vdw}	ΔE_{ele}	ΔG_{pol}	ΔG_{nonpol}
Diosgenin – HIV-1	-34.59 ± 0.11	-40.67 ± 0.12	0.58 ± 0.15	9.58 ± 0.17	-4.08 ± 0.02
Cyclopiazonic – HIV-1	-29.30 ± 0.44	-36.64 ± 0.09	-9.52 ± 0.39	21.03 ± 0.23	-4.18 ± 0.01
Aflatoxin B1 – HIV-1	-25.66 ± 0.21	-31.26 ± 0.28	-2.27 ± 0.71	11.79 ± 0.31	-3.91 ± 0.01
ORV – HIV-1	-47.75 ± 0.12	-56.85 ± 0.11	-33.67 ± 0.15	50.61 ± 0.14	-7.84 ± 0.01

Table 6. Binding free energy contributions for HIV-1 protease ligand complexes. ΔG_{bind} —binding free energy; ΔE_{ele} —electrostatic interaction; ΔE_{vdw} —van der Waals forces; ΔG_{pol} —polar solvation energy; ΔG_{nonpol} —nonpolar solvation energy.

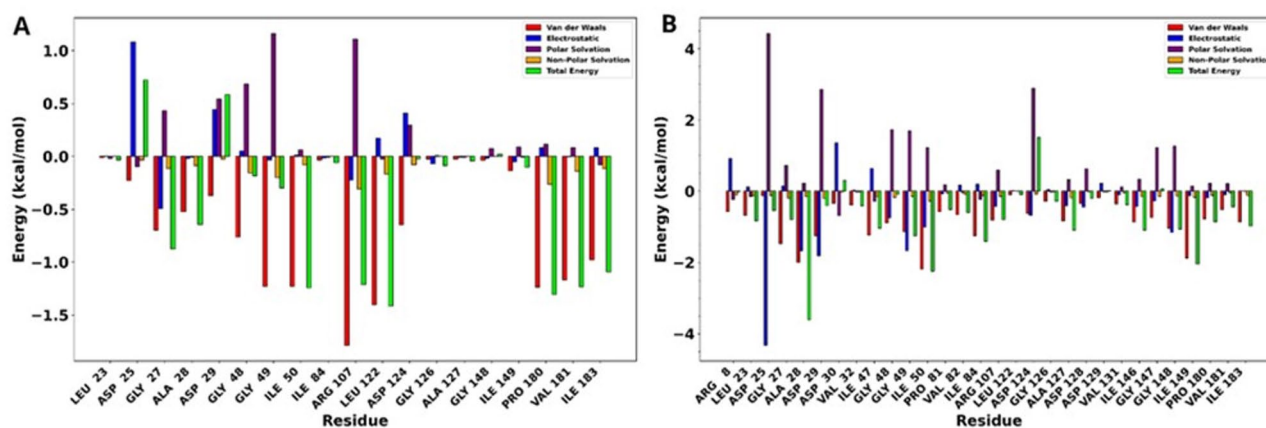


Fig. 13. Per-residue energy decomposition plots showing the contributions to the binding and stabilisation of (A) diosgenin and (B) ORV in the HIV-1 protease active site during 200 ns molecular dynamics simulations.

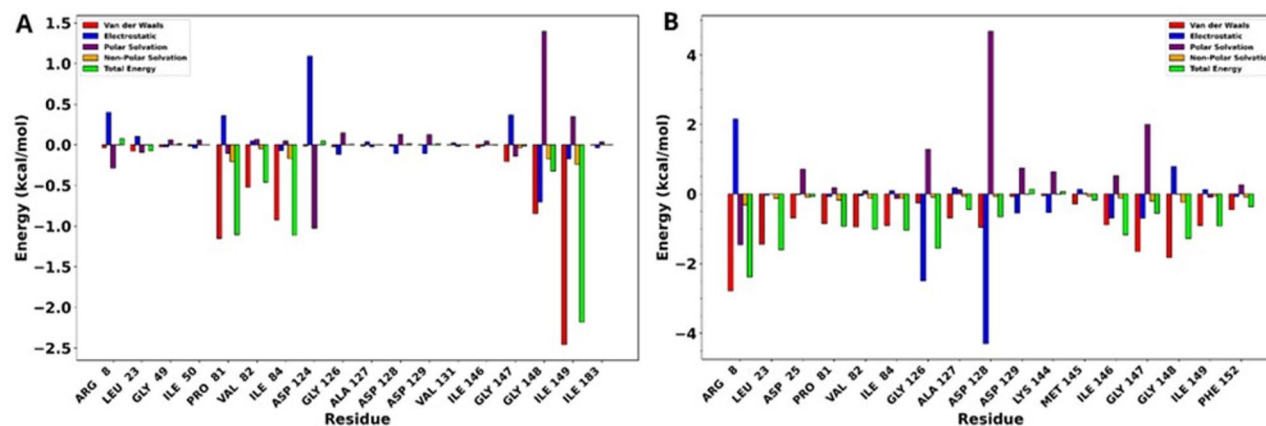


Fig. 14. Per-residue energy decomposition plots showing the contributions to the binding and stabilization of (A) aflatoxin B1 and (B) cyclopiazonic acid in the HIV-1 protease active site during 200 ns molecular dynamics simulations.

plant leaves inhibited two distinct HIV-1 subtype strains⁴⁶. The results from our virtual screening and molecular interaction studies demonstrate the potential of diosgenin as the most effective protease inhibitor among the analysed compounds. The post-MD analysis comprehensively evaluated the binding characteristics of four ligands, with diosgenin emerging as the most promising candidate. Structural stability metrics provided the first indication of diosgenin's superior performance. The compound demonstrated the lowest RMSD of 1.16 Å and RMSF of 0.86 Å, significantly lower than other studied compounds. These values directly translate to minimal conformational fluctuations and superior binding stability. The radius of gyration of 8.47 Å further validated these findings, revealing a tightly packed protein conformation that suggests robust interactions within the binding pocket.

Hydrogen bonding and solvent interactions offered additional insights into diosgenin's molecular behaviour. The compound maintained a moderately stable hydrogen bond network of 2.93 bonds and displayed a relatively

low SASA value of 741 Å². These characteristics indicate optimal pocket occupancy and limited solvent exposure, further reinforcing its potential as an effective ligand. Binding energy calculations provided quantitative evidence of diosgenin's efficacy. The compound demonstrated a strong affinity for the target protein with a binding free energy (ΔG_{bind}) of -34.59 ± 0.11 kcal/mol, primarily driven by hydrophobic interactions. Principal component analysis complemented these findings, revealing constrained dynamics with minimal conformational variability.

In comparison, cyclopiazonic acid showed slightly less favourable characteristics. With marginally higher RMSD (1.33 Å) and RMSF (0.88 Å) values, and a less favourable binding free energy (ΔG_{bind}) of -29.61 ± 0.09 kcal/mol, the compound exhibited fewer stable interactions compared to diosgenin. Aflatoxin B1 presented the most challenging molecular profile. Its high RMSD (1.54 Å) and RMSF (0.99 Å) values indicated significant structural flexibility and instability. The binding free energy (ΔG_{bind}) of -25.66 ± 0.21 kcal/mol, combined with expansive conformational variability, suggested the weakest protein-ligand interactions among the studied compounds. Diosgenin outperformed the other compounds regarding stability, binding energy, and protein-ligand interaction patterns, making it a compelling candidate for further research and development. These findings offer a promising avenue for exploring natural product-derived compounds from endophytic fungi like *P. rubens*.

P. rubens has been established as an industrial producer of penicillin, a β -lactam antibiotic⁴⁷. Its role as a penicillin producer has placed this prolific species in the limelight of biotechnological interest in producing secondary metabolites⁴⁸. In addition, this has led to the species being the most extensively studied amongst its genus of more than 350 *Penicillium* species for novel secondary metabolites with medicinal potential^{48,49}. However, very few studies have evaluated and reported on its production of secondary metabolites with anti-HIV properties, particularly secondary metabolites with anti-HIV-1 properties. For example, Bringmann et al.⁸ described a novel sorbicillinoid alkaloid (Sorbicillatone A) to demonstrate significant antiviral activity on the expression of HIV viral proteins.

Conclusion

The observed variances in the production of secondary metabolites with antiviral activities from different media indicated the role played by different stimuli in these media to mimic the conditions in the natural environment that awaken silent BGCs. The most promising compounds with anti-HIV activity were observed in oat media. The MM-GBSA ΔG_{bind} calculations revealed diosgenin as the most promising compound, with a favourable binding free energy of -34.59 kcal/mol. This underscores its strong binding potential and stability within the protease active site. These findings emphasize the biosynthetic abilities of *P. rubens* cultivated in oats media as a good source of anti-HIV-1 secondary metabolites.

Data availability

The positive Feature-Based Molecular Networking data is available at <https://gnps.ucsd.edu/ProteoSAFe/status.jsp?task=79673f544bdd4bf0b31bf915f7a5b14f>. The LC-HRMS/MS metabolomics data has been deposited in Massive <https://massive.ucsd.edu/ProteoSAFe/dataset.jsp?accession=MSV000097382>.

Received: 19 January 2025; Accepted: 18 June 2025

Published online: 02 July 2025

References

- McLaren, P. J. & Fellay, J. HIV-1 and human genetic variation. *Nat. Rev. Genet.* **22**, 645–657. <https://doi.org/10.1038/s41576-021-0378-0> (2021).
- Nzimande, B., Makhwitine, J. P., Mkhwanazi, N. P. & Ndlovu, S. I. Developments in Exploring Fungal Secondary Metabolites as Antiviral Compounds and Advances in HIV-1 Inhibitor Screening Assays. *Viruses-Basel* **15** (2023). <https://doi.org/10.3390/v15051039>.
- Andrae-Marobela, K., Ghislain, F. W., Okatch, H. & Majinda, R. R. Polyphenols: a diverse class of multi-target anti-HIV-1 agents. *Curr. Drug Metab.* **14**, 392–413. <https://doi.org/10.2174/13892002113149990095> (2013).
- Adamson, C. S. et al. Correction: Antiviral drug discovery: Preparing for the next pandemic. *Chem. Soc. Rev.* **50**, 9346. <https://doi.org/10.1039/d1cs90064a> (2021).
- Fanele, A. & Ndlovu, S. I. Endophytic fungal species *Nigrospora oryzae* and *Alternaria alternata* exhibit antimicrobial activity against gram-positive and gram-negative multi-drug resistant clinical bacterial isolates. *BMC Complement. Med. Ther.* **23**, 323. <https://doi.org/10.1186/s12906-023-04157-8> (2023).
- Strobel, G. & Daisy, B. Bioprospecting for microbial endophytes and their natural products. *Microbiol. Mol. Biol. R.* **67**, 491–. <https://doi.org/10.1128/Mmbr.67.4.491-502.2003> (2003).
- Gouda, S. et al. A treasure house of bioactive compounds of medicinal importance. *Front. Microbiol.* **7**, 1538. <https://doi.org/10.3389/fmicb.2016.01538> (2016).
- Bringmann, G. et al. The first sorbicillinoid alkaloids, the antileukemic sorbicillactones A and B, from a sponge-derived strain. *Tetrahedron* **61**, 7252–7265. <https://doi.org/10.1016/j.tet.2005.05.026> (2005).
- Makhwitine, J. P., Kumalo, H. M., Ndlovu, S. I. & Mkhwanazi, N. P. Epigenetic Induction of Secondary Metabolites Production in Endophytic Fungi *Penicillium chrysogenum* and GC-MS Analysis of Crude Metabolites with Anti-HIV-1 Activity. *Microorganisms* **11** <https://doi.org/ARTN1404> (2023).
- 3390/microorganisms11061404 10 et al. OSMAC-Based discovery and biosynthetic gene clusters analysis of secondary metabolites from Marine-Derived *Streptomyces globisporus* SCSIO LCY30. *Mar. Drugs.* **22** <https://doi.org/10.3390/md22010021> (2023).
- Chervin, J. et al. Dereplication of natural products from complex extracts by regression analysis and molecular networking: case study of redox-active compounds from *Viola Alba* subsp. *Dehnhardtii*. *Metabolomics* **13**, 1–12 (2017).
- Wennrich, J. P. et al. Bioactive naphtho- α -pyranones from two endophytic fungi of the genus *polyphilus*. *Antibiotics* **12**, 1273 (2023).
- Stoszko, M. et al. Gliotoxin, identified from a screen of fungal metabolites, disrupts 7SK snrnp, releases P-TEFb, and reverses HIV-1 latency. *Sci. Adv.* **6**, eaba6617. <https://doi.org/10.1126/sciadv.aba6617> (2020).
- Schmid, R. et al. Integrative analysis of multimodal mass spectrometry data in MZmine 3. *Nat. Biotechnol.* **41**, 447–449. <https://doi.org/10.1038/s41587-023-01690-2> (2023).

15. Wang, M. et al. Sharing and community curation of mass spectrometry data with global natural products social molecular networking. *Nat. Biotechnol.* **34**, 828–837. <https://doi.org/10.1038/nbt.3597> (2016).
16. Nthias, L. F. et al. Feature-based molecular networking in the GNPS analysis environment. *Nat. Methods.* **17**, 905–908 (2020).
17. Horai, H. et al. MassBank: a public repository for sharing mass spectral data for life sciences. *J. Mass. Spectrom.* **45**, 703–714. <https://doi.org/10.1002/jms.1777> (2010).
18. Mohimani, H. et al. Dereplication of microbial metabolites through database search of mass spectra. *Nat. Commun.* **9**, 4035. <https://doi.org/10.1038/s41467-018-06082-8> (2018).
19. Dührkop, K. et al. SIRIUS 4: a rapid tool for turning tandem mass spectra into metabolite structure information. *Nat. Methods.* **16**, 299–302. <https://doi.org/10.1038/s41592-019-0344-8> (2019).
20. Dührkop, K., Shen, H., Meusel, M., Rousu, J. & Bocker, S. Searching molecular structure databases with tandem mass spectra using csi:fingerid. *Proc. Natl. Acad. Sci. U S A.* **112**, 12580–12585. <https://doi.org/10.1073/pnas.1509788112> (2015).
21. Dührkop, K. et al. Systematic classification of unknown metabolites using high-resolution fragmentation mass spectra. *Nat. Biotechnol.* **39**, 462–471. <https://doi.org/10.1038/s41587-020-0740-8> (2021).
22. Pakkiri Shah, A. K. et al. Statistical analysis of feature-based molecular networking results from non-targeted metabolomics data. *Nat. Protoc.* <https://doi.org/10.1038/s41596-024-01046-3> (2024).
23. Shannon, P. et al. Cytoscape: a software environment for integrated models of biomolecular interaction networks. *Genome Res.* **13**, 2498–2504. <https://doi.org/10.1101/gr.1239303> (2003).
24. Morris, G. M. et al. AutoDock4 and AutoDockTools4: automated Docking with selective receptor flexibility. *J. Comput. Chem.* **30**, 2785–2791. <https://doi.org/10.1002/jcc.21256> (2009).
25. O’Boyle, N. M. et al. Open babel: an open chemical toolbox. *J. Cheminform.* **3**, 33. <https://doi.org/10.1186/1758-2946-3-33> (2011).
26. Eberhardt, J., Santos-Martins, D., Tillack, A. F. & Forli, S. AutoDock Vina 1.2.0: new Docking methods, expanded force field, and Python bindings. *J. Chem. Inf. Model.* **61**, 3891–3898. <https://doi.org/10.1021/acs.jcim.1c00203> (2021).
27. Trott, O. & Olson, A. J. AutoDock vina: improving the speed and accuracy of Docking with a new scoring function, efficient optimization, and multithreading. *J. Comput. Chem.* **31**, 455–461. <https://doi.org/10.1002/jcc.21334> (2010).
28. Dassault, S. v. *v21.1.0.20298* (Dassault Systèmes, 2024).
29. Schrödinger, L. & DeLano, W. P. M. O. L. (2020). Available from: <http://www.pymol.org/pymol>
30. Ben-Shalom, I. Y., Lin, C., Radak, B. K., Sherman, W. & Gilson, M. K. Fast equilibration of water between buried sites and the bulk by molecular dynamics with parallel Monte Carlo water moves on graphical processing units. *J. Chem. Theory Comput.* **17**, 7366–7372. <https://doi.org/10.1021/acs.jctc.1c00867> (2021).
31. Du, Q. Q., Qian, Y. & Xue, W. W. Cross-reactivity of two human IL-6 family cytokines OSM and LIF explored by protein-protein docking and molecular dynamics simulation. *Bba-Gen Subjects* 1865 (2021). <https://doi.org/10.1016/j.bbagen.2021.129907>.
32. Fakhar, Z., Hejazi, L., Tabatabai, S. A. & Munro, O. Q. Discovery of novel heterocyclic amide-based inhibitors: an integrative in-silico approach to targeting soluble epoxide hydrolase. *J. Biomol. Struct. Dyn.* **40**, 7114–7128. <https://doi.org/10.1080/07391102.2021.1894987> (2022).
33. Li, Y. A. et al. Discovery of a small molecule inhibitor of Cullin neddylation that triggers ER stress to induce autophagy. *Acta Pharm. Sin B.* **11**, 3567–3584. <https://doi.org/10.1016/j.apsb.2021.07.012> (2021).
34. Wolf, S. et al. Hierarchical dynamics in allostery following ATP hydrolysis monitored by single molecule FRET measurements and MD simulations. *Chem. Sci.* **12**, 3350–3359. <https://doi.org/10.1039/d0sc06134d> (2021).
35. Panwar, A. K. In-silico analysis and molecular dynamics simulations of lysozyme by GROMACS. *Ann. Rom Soc. Cell. Biol.* **25**, 9679–9685 (2021).
36. Jin, T. Y., Patel, S. J. & Van Lehn, R. C. Molecular simulations of lipid membrane partitioning and translocation by bacterial quorum sensing modulators. *Plos One* **16** (2021).
37. Xu, L., Sun, H., Li, Y., Wang, J. & Hou, T. Assessing the performance of MM/PBSA and MM/GBSA methods. 3. The impact of force fields and ligand charge models. *J. Phys. Chem. B.* **117**, 8408–8421. <https://doi.org/10.1021/jp404160y> (2013).
38. Kollman, P. A. et al. Calculating structures and free energies of complex molecules: combining molecular mechanics and continuum models. *Acc. Chem. Res.* **33**, 889–897. <https://doi.org/10.1021/ar000033j> (2000).
39. Massova, I. & Kollman, P. A. Combined molecular mechanical and continuum solvent approach (MM-PBSA/GBSA) to predict ligand binding. *Perspect. Drug Discov.* **18**, 113–135. <https://doi.org/10.1023/A:1008763014207> (2000).
40. Chigayo, K., Mojapelo, P. E. L., Mnyakeni-Moleele, S. & Misihairabgwi, J. M. Phytochemical and antioxidant properties of different solvent extracts of *Kirkia wilmsii* tubers. *Asian Pac. J. Trop. Biomed.* **6**, 1037–1043 (2016).
41. Li, H., Booth, T. & Chooi, Y. H. in *Comprehensive Natural Products III: Chemistry and Biology* 415–444 Elsevier, (2020).
42. Singh, P., Sharma, A. & Nandi, S. P. Identification of potent inhibitors of covid-19 main protease enzyme by molecular Docking study. (2020).
43. Chen, J. H. et al. Reduced lysosomal density in neuronal dendrites mediates deficits in synaptic plasticity in huntington’s disease. *Cell Reports* **42** (2023).
44. Cui, R. et al. Cyclopiazonic acid, an inhibitor of calcium-dependent ATPases with antiviral activity against human respiratory syncytial virus. *Antiviral Res.* **132**, 38–45. <https://doi.org/10.1016/j.antiviral.2016.05.010> (2016).
45. Huang, N., Yu, D., Wu, J. & Du, X. Diosgenin: an important natural pharmaceutical active ingredient. *Food Sci. Technol.* **42**, e94521 (2021).
46. Rakshit, S. et al. Role of Diosgenin extracted from *Helicteres Isora* L in suppression of HIV-1 replication: an in vitro preclinical study. *Heliyon* **10** (2024).
47. Wu, M., Crismaru, C. G., Salo, O., Bovenberg, R. A. L. & Driessen, A. J. M. Impact of classical strain improvement of penicillium Rubens on amino acid metabolism during β -Lactam production. *Appl. Environ. Microbiol.* **86** <https://doi.org/10.1128/aem.01561-19> (2020).
48. Fierro, F., Vaca, I., Castillo, N. I., García-Rico, R. O. & Chávez, R. Penicillium chrysogenum, a vintage model with a cutting-edge profile in biotechnology. *Microorganisms* **10**, 573 (2022).
49. Guzmán-Chávez, F., Zwahlen, R. D., Bovenberg, R. A. L. & Driessen, A. J. M. Engineering of the filamentous fungus penicillium chrysogenum as cell factory for natural products. *Front. Microbiol.* **9**, 2768. <https://doi.org/10.3389/fmicb.2018.02768> (2018).

Acknowledgements

The authors would like to acknowledge the Center for High Performance Computing, South Africa, for providing access to the computing infrastructure.

Author contributions

Conceptualization: S.I.N Methodology: S.I.N, N.P.M, W.P.N and S.E.M Data analysis: N.N.M, M.C.K, S.I.N and S.E.M Investigation: N.N.M., M.C.K and S.E.M Original draft preparation: N.N.M and S.I.N Review and editing: N.N.M, M.C.K, N.P.M, S.E.M and S.I.N Supervision: N.P.M and S.I.N Project administration: S.I.N Funding acquisition: N.P.M and S.I.N.

Funding

The National Research Foundation funded the work under the Thuthuka Grant number 129778 received by SIN. NMM was funded by the Poliomyelitis Research Foundation (PRF) and Connect Africa scholarships.

Declarations

Competing interests

The authors declare no competing interests.

Additional information

Supplementary Information The online version contains supplementary material available at <https://doi.org/10.1038/s41598-025-08091-2>.

Correspondence and requests for materials should be addressed to S.I.N.

Reprints and permissions information is available at www.nature.com/reprints.

Publisher's note Springer Nature remains neutral with regard to jurisdictional claims in published maps and institutional affiliations.

Open Access This article is licensed under a Creative Commons Attribution-NonCommercial-NoDerivatives 4.0 International License, which permits any non-commercial use, sharing, distribution and reproduction in any medium or format, as long as you give appropriate credit to the original author(s) and the source, provide a link to the Creative Commons licence, and indicate if you modified the licensed material. You do not have permission under this licence to share adapted material derived from this article or parts of it. The images or other third party material in this article are included in the article's Creative Commons licence, unless indicated otherwise in a credit line to the material. If material is not included in the article's Creative Commons licence and your intended use is not permitted by statutory regulation or exceeds the permitted use, you will need to obtain permission directly from the copyright holder. To view a copy of this licence, visit <http://creativecommons.org/licenses/by-nc-nd/4.0/>.

© The Author(s) 2025